Modelling and simulation of hydrodynamics in double loop circulating fluidized bed reactor for chemical looping combustion process

Yuanwei Zhang[a,*], Zhongxi Chao[b], Hugo A. Jakobsen[a]

[a]*Department of Chemical engineering, Norwegian University of Science and Technology, Sem Sælandsvei 4, 7034 Trondheim, Norway*
[b]*Safetec Nordic AS, Klæbuveien 194, 7037 Trondheim, Norway*

Abstract

A multiphase CFD model has been developed and implemented in an in-house code for a coupled double loop circulation fluidized bed (DLCFB) reactor which can be utilized for the chemical looping combustion process. The air reactor and the fuel reactor were operated in fast fluidization regime and simulated separately, the connection between the two reactors is realized through specific inlet and outlet boundary conditions. This work represents a first attempt to model and simulate the novel DLCFB system. The model predictions of the axial pressure profiles are in good agreement with the experimental data reported in the literatures. In addition, typical core-annulus structure of radial solid volume fraction distribution can be well predicted in both reactors. These indicate the capability of the model for predicting the cold flow performance of the DLCFB system. Furthermore, the effects of superficial gas velocity, total solid inventory on the flow characteristics have been examined. The results show that an increase of the gas velocity could enhance the solid exchanges between the two reactors. The additional solids were accumulated in the bottom of the reactors when the total solid inventory was increased.

Keywords: Double loop circulating fluidized bed; CFD model for circulating

*Corresponding author
Email addresses: `yuanwei.zhang@ntnu.no` (Yuanwei Zhang), `Phone number:`
`47-98465832` (Yuanwei Zhang)

fluidized bed; Kinetic theory of granular flow; Hydrodynamics

---

1. Introduction

Over the past decades, global warming has caused significant negative impacts on the natural and human system. There is an overwhelming consensus among scientists that the anthropogenic emissions of carbon dioxide (CO_2) are the major contributor to the warming trend. That is why a tremendous number of technologies have been advocated to reduce the CO_2 emission, especially from the energy sector.

Carbon Capture and Storage (CCS) is a promising technology for reducing CO_2 emissions because of the increasing fossil fuel consumption and the domination of carbon-intensive industries.[1] The CCS technology can be divided into four groups as pre-combustion, oxy-fuel combustion, post-combustion and chemical looping combustion (CLC). Since the first three ones will result in a drop in process efficiency and high energy penalty[2], CLC has drawn more and more attention.

CLC is a novel combustion process with two successive reaction systems forming a chemical loop instead of the conventional combustion reaction system. The process primarily consists of two fluidized bed reactors, the fuel reactor (FR) and the air reactor (AR). In the FR, the fuel reacts with the metal oxide which is called an oxygen carrier (OC) to produce CO_2 and H_2O. H_2O can then be removed by condensation and only carbon dioxide is remaining for storage. The oxygen carrier is being reduced from MeO_α to $MeO_{\alpha-1}$ and transported to the AR. In the AR the $MeO_{\alpha-1}$ oxidized to MeO_α by oxygen of the air and circulating back to FR. In this way, the mixing of fuel and air is avoided and CO_2 will inherently not be diluted with nitrogen which would otherwise require high energy cost. More detailed descriptions of the development of the CLC process can be found in several review articles [2–4].

In recent years computational fluid dynamics (CFD) has become a useful tool for studying the fluidized bed system. There are two modelling frame-

works for modelling the gas-solid flow, the Eulerian - Lagrangian (E-L) model and the Eulerian - Eulerian model, also known as the two-fluid model. Due to the high computational resources required for solving the E-L model, most researches choose the two-fluid model for studying the fluidized bed reactor. In this method, which is also used in this work, both phases are described as interpenetrating continua and modelled in the framework of the Navier-Stockes equations using averaging quantities.

CFD simulations by use of the two-fluid model for describing the CLC process have been employed in several articles. The first attempt was made by Jung and Gamwo [5] followed by Deng et al [6, 7] and Jin et al.[8] In their simulations, the typical bubble behaviour and flow patten were observed but no experimental data were available for the model validation. Moreover low fuel gas conversions were predicted due to the bubbles formed and the reacting gas bypassing the solid inside the bubbling bed. Kruggel-Emden et al.[9], Mahalatkar et al.[10] also conducted studies of the reactive performance of the CLC system. The simulation studies mentioned above were limited to the fuel reactor only, but a few authors have also carried out the full loop simulation of the CLC process.

Kruggel-Emden et al.[11] applied the exchanges of solid mass through a time-dependent inlet and outlet boundary coupled to the fuel and air reactors, the developed interconnected CFD model shows promising results for developments of the CLC process. Wang et al.[12], Ahmed and Lu [13], Su et al. [?] and Banerjee et al. [14] studied the CLC process by developing a 2D full loop CFD model and successfully predicted the hydrodynamic characteristics. Besides the 2D models, 3D models have also employed by Guan et al.[15] and Geng et al.[16] for hydrodynamic studies. The 3-D CLC simulation combining hydrodynamics and reaction kinetics was carried out by Parker [17] and Banerjee et al. [14].

Up to date, most numerical studies were performed on a typical configuration which consists of a high velocity riser as the AR and a low velocity bubbling fluidized bed as the FR. Only a few attempts [12, 18, 19] were made for other reactor designs. In order to get sufficiently high solid circulation rate and fuel conversion, enhance gas-solid contact and realize flexible operation,

3

SINTEF Energy Research and the Norwegian University of Science and Technology have designed a double loop circulating fluidized bed (DLCFB) reactor for CLC process[20]. This system is modelled and simulated in this work. In their DLCFB system, which is sketched in Figure 1 (a), the air reactor as well as the fuel reactor were operated as a circulating fluidized bed reactor. The interconnection between the reactor units was realized by means of two divided loop-seals and a bottom extraction/lift. The loop-seals are fluidized through three bubble caps (central, external and internal) so that the solids entrained by one reactor can be lead into the other reactor or re-circulated back into the original one. During the experiment, the solid outflow from one reactor is injected into the bottom of the other reactor through the cyclones and external loop-seals.

Proper understanding of the complex gas-solid hydrodynamic characteristics of the DLCFB reactor is required for providing guidance in the design and operation of the CLC reactor system. In the present work, a multiphase CFD model for an interconnected DLCFB reactor has been developed and implemented using the Fortran programming language. The main objective of this investigation is to validate the model and to explore the hydrodynamic behaviours of the system under different operational conditions.

2. Multiphase fluid dynamics model

This section presents the governing equations for each phase as well as the constitutive closure models. For the gas phase, the transport equations can be derived by applying a suitable averaging procedure to the local instantaneous equations[21], while the transport equations for solid phase originate from the ensemble average of a single-particle quantity over the Boltzmann integral-differential equation[22].

4

2.1. Continuity equations

The continuity equations for the gas phase and solid phase are given as
follows:

$$\frac{\partial}{\partial t}(\alpha_g \rho_g) + \nabla \cdot (\alpha_g \rho_g \vec{v}_g) = 0 \tag{1}$$

$$\frac{\partial}{\partial t}(\alpha_s \rho_s) + \nabla \cdot (\alpha_s \rho_s \vec{v}_s) = 0 \tag{2}$$

The volume fraction of gas phase (α_g) and solid phase (α_s) are sum up to one
in the two-phase model:

$$\alpha_g + \alpha_s = 1 \tag{3}$$

2.2. momentum equations

The momentum equations for the gas and solid phases can be expressed by:

$$\frac{\partial}{\partial t}(\alpha_g \rho_g \vec{v}_g) + \nabla \cdot (\alpha_g \rho_g \vec{v}_g \vec{v}_g) = -\alpha_g \nabla p - \nabla \cdot \alpha_g \bar{\bar{\tau}}_g + \vec{M}_g + \alpha_g \rho_g \vec{g} \tag{4}$$

$$\frac{\partial}{\partial t}(\alpha_s \rho_s \vec{v}_s) + \nabla \cdot (\alpha_s \rho_s \vec{v}_s \vec{v}_s) = -\alpha_s \nabla p - \nabla \cdot \alpha_s \bar{\bar{\tau}}_s + \vec{M}_s + \alpha_s \rho_s \vec{g} \tag{5}$$

2.3. Turbulence model for the gas phase

A standard $\kappa - \varepsilon$ turbulence model [23, 24] has been used to describe the tur-
bulence phenomena in the gas phase, the gas turbulent kinetic energy equation
is expressed by:

$$\frac{\partial}{\partial t}(\alpha_g \rho_g k_g) + \nabla \cdot (\alpha_g \rho_g k_g \vec{v}_g) = \alpha_g(-\bar{\bar{\tau}}_t : \nabla \vec{v}_g + S_t) \\ + \nabla \cdot (\alpha_g \frac{\mu_{g,t}}{\sigma_g} \nabla k_g) - \alpha_g \rho_g \varepsilon_g \tag{6}$$

The turbulent energy dissipation rate equation is formulated as:

$$\frac{\partial}{\partial t}(\alpha_g \rho_g \varepsilon_g) + \nabla \cdot (\alpha_g \rho_g \varepsilon_g \overrightarrow{v}_g) = \alpha_g C_1 \frac{\varepsilon_g}{k_g}(-\bar{\bar{\tau}}_t : \nabla \overrightarrow{v}_g + S_t)$$
$$+ \nabla \cdot (\alpha_g \frac{\mu_{g,t}}{\sigma_\varepsilon} \nabla \varepsilon_g) - \alpha_g \rho_g C_2 \frac{\varepsilon_g^2}{k_g} \tag{7}$$

2.4. Constitutive Closure Models

2.4.1. Inter-phase drag model

The two phases are coupled through the interfacial momentum transfer, which is dominated by the drag force. In this study, the Gibilaro [25] drag model was used. The cluster effect inside the riser is modelled by use of the method proposed by McKeen and Pugsley [26]. The interfacial drag force is thus modelled as:

$$\overrightarrow{M}_g = -\overrightarrow{M}_s = C\overrightarrow{F}_D = C\beta(\overrightarrow{v_s} - \overrightarrow{v_g}) \tag{8}$$

The value of the calibration parameter C is different for different kinds of particles. It is used as a tuning parameter to match the simulation results with the experimental pressure and solid volume fraction data. For the particle used in the DLCFB reactor system, the value C is 0.4. The friction factor is given by [25]:

$$\beta = \left(\frac{17.3}{Re_p + 0.336}\right)\frac{\rho_g \mid \overrightarrow{v_s} - \overrightarrow{v_g} \mid}{d_p}\alpha_s \alpha_g^{-1.8} \tag{9}$$

where the particle Reynolds number is:

$$Re_p = \frac{d_p \alpha_g \rho_g |\overrightarrow{u}_g - \overrightarrow{u}_s|}{\mu_g} \tag{10}$$

2.4.2. Closure Model for the gas phase

The gas phase viscous stress tensor in equation (4) is given as:

$$\bar{\bar{\tau}}_g = -\mu_g \left(\nabla \overrightarrow{v}_g + (\nabla \overrightarrow{v}_g)^T - \frac{2}{3}(\nabla \cdot \overrightarrow{v}_g)\bar{\bar{\mathrm{I}}}\right) \tag{11}$$

6

113 in which the bulk viscosity of the continuous gas was set to zero.

114   In the turbulence model, turbulent viscosity is defined by:

$$\mu_{g,t} = \rho_g C_\mu \frac{k_g^2}{\varepsilon_g} \tag{12}$$

115   The turbulent kinetic energy production S_t due to the motion of the particles
116 can be modelled with the method proposed by [27]:

$$S_t = C_b \beta (\vec{v}_s - \vec{v}_g)^2 \tag{13}$$

117   The turbulent stress tensor is modelled by using the gradient- and Boussinesq
118 hypotheses[24]:

$$\bar{\bar{\tau}}_t = -\frac{2}{3}\rho_g k_g \bar{\bar{\mathrm{I}}} + \mu_{g,t}\left(\nabla \vec{v}_g + (\nabla \vec{v}_g)^T - \frac{2}{3}(\nabla \cdot \vec{v}_g)\bar{\bar{\mathrm{I}}}\right) \tag{14}$$

119   The empirical parameters in the $\kappa - \varepsilon$ turbulence model are given in Table
120 1.

121 *2.4.3. Kinetic theory of granular flow*

122   When the solid phase is treated as a fluid in the two-fluid model, some
123 physical properties like solid pressure, solid viscosity are missing. The kinetic
124 theory of granular flow (KTGF) [28] was used to derive the different physical
125 properties of the solid phase. In this method, the granular temperature, which
126 is a statistical measure of the fluctuating kinetic energy of the particles, was
127 introduced and can be expressed as:

$$\frac{3}{2}\left[\frac{\partial}{\partial t}(\alpha_s \rho_s \Theta_s) + \nabla \cdot (\alpha_s \rho_s \Theta_i \vec{v}_s)\right] = -\bar{\bar{\tau}}_s : \nabla \vec{v}_s + \nabla \cdot (\kappa_s \nabla \Theta_s)$$
$$- 3\beta\Theta_s - \gamma_s \tag{15}$$

128   The conductivity of the granular temperature is calculated from [29]:

$$\kappa_s = \frac{15}{2}\frac{\mu_s^{dilute}}{(1+e)g_0}\left[1 + \frac{6}{5}\alpha_s g_0(1+e)\right]^2 + 2\alpha_s^2 \rho_s d_p(1+e)g_0\sqrt{\frac{\Theta_s}{\pi}} \tag{16}$$

7

The collisional energy dissipation term is given by [30]

$$\gamma_s = 3(1 - e^2)\alpha_s^2 \rho_s g_0 \Theta_s \left[\frac{4}{d_p}\sqrt{\frac{\Theta_s}{\pi}} - \nabla \cdot \vec{v}_s \right] \tag{17}$$

The radial distribution function denote the average distance between particles and is calculated from an empirical relation[31]

$$g_0 = \frac{1 + 2.5\alpha_s + 4.5904\alpha_s^2 + 4.515439\alpha_s^3}{\left[1 - (\frac{\alpha_s}{\alpha_s^{max}})^3 \right]^{0.67802}} \tag{18}$$

The total pressure tensor of the solid phase occurring in (5) and (15) is modelled similar to the Newton's viscosity law:

$$\bar{\bar{\tau}}_s = -(-p_s + \alpha_s \mu_{B,s} \nabla \cdot \vec{v}_s) - \alpha_s \mu_s \left(\nabla \vec{v}_s + (\nabla \vec{v}_s)^T - \frac{2}{3}(\nabla \cdot \vec{v}_s)\bar{\bar{I}} \right) \tag{19}$$

where the solid pressure p_s and the bulk viscosity $\mu_{B,s}$ is taken from [32]:

$$p_s = \alpha_s \rho_s \Theta_s [1 + 2(1 - e)\alpha_s g_0] \tag{20}$$

$$\mu_{B,s} = \frac{4}{3}\alpha_s \rho_s d_p g_0 (1 + e)\sqrt{\frac{\Theta_s}{\pi}} + \frac{4}{5}\alpha_s \rho_s d_p g_0 (1 + e) \tag{21}$$

The solid phase shear viscosity can be modelled following the approach by [29]

$$\mu_s = \frac{2\mu_s^{dilute}}{\alpha_s g_0 (1 + e)} \left[1 + \frac{4}{5}\alpha_s g_0 (1 + e) \right]^2 + \frac{4}{5}\alpha_s \rho_s g_0 (1 + e)\sqrt{\frac{\Theta_s}{\pi}} \tag{22}$$

in which the dilute viscosity μ_s^{dilute} is expressed by:

$$\mu_s^{dilute} = \frac{5}{96}\rho_s d_p \sqrt{\pi \Theta_s} \tag{23}$$

8

3. Interconnected model and numerical considerations

3.1. Geometry of the reactors and the definition of the computational domain

In the DLCFB system, the air reactor as well as the fuel reactor are operated in the fast fluidization regime in order to raise the fuel conversion with a better gas-solid contact of the upper part of the rector. Both reactors are 5 m heigh while the diameter of AR and FR are 0.23 m and 0.144 m, respectively. The graphical representation of this architecture can be found in [20]. The 2D plane geometry was chosen for the simulation of the two reactors, which is sketched in Figure 1 (b), having the same dimensions as the experimental setup. The computational domain was meshed by using uniform grids in each direction. Three different grid sizes (0.006 × 0.027 m, 0.0048 × 0.02 m, 0.004 × 0.016 m) were examined. The corresponding results are shown in Figure 2. It can be seen that the pressure profile predicted by the coarse grid is somewhat higher than the other two in the lower part of the reactors. However, overall no obvious differences are observed comparing the results for the three gird sizes. Considering the simulation time and the numerical accuracy, the medium grid (0.0048 × 0.02 m) was used in this study.

3.2. Combination of two reactors

Two different sets of coordinates and parameters were adopted to solve the governing equations for the AR and the FR, respectively. The solid flowing out of the AR is fed into the bottom of the FR, and in the similar way all the solids that exited at the outlet of FR will be injected into the bottom of the AR. The exchange of the solid flow between the reactor units were realized through the time-dependent inlet and outlet boundary conditions. At each simulation time step, the processes in the two risers were simulated separately, the solid flux of the inlet of one riser was calculated from the solid flowing out of the outlet of the other riser. In the experimental rig, this kind of continuous solid exchange is achieved by means of cyclones and divided loop-seals. The cyclones are neglected in the simulation by assuming the efficiency of cyclone is

9

equal to one. The bottom extraction/lift is replaced by an internal recirculation mechanism in order to keep the mass balance inside one reactor. In this way, a full loop was fulfilled for one time step. Then, another computation loop for next time step will run repeatedly.

3.3. Initial and Boundary conditions

Initially, there is no gas flow in the reactor and the bed is at rest with a particle volume fraction of 0.6. A uniform gas plug flow is applied at the inlets of the reactors, the inlet solid flux of one of the reactors was kept consistent with the outlet solid flux of the other one with a prescribed solid volume fraction at the inlet. The normal velocities at all boundaries are set to zero. The no-slip wall boundary condition was set for the gas phase while the solids were allowed to slip along the wall, following the equation (24) from [24].

$$\vec{v}_{s,z}|_{wall} = \frac{d_p}{\alpha_s^{1/3}} \frac{\partial \vec{v}_{s,z}}{\partial r} \tag{24}$$

where $\vec{v}_{s,z}$ is the axial velocity of the particles. r indicates the radial direction.

For all scalar variables but pressure, Dirichlet boundary conditions are used at the inlet, while Neumann conditions are used at the other boundaries. For the pressure correction equations, all the boundaries except outlet were adopted Neumann conditions. At the outlet a fixed pressure is specified.

3.4. Numerical Procedure

The two-fluid model equations were discretized by the finite volume method and implemented in an in-house code. The algorithm is based on the work by Lindborg [23] and Jakobsen[24]. The second order central differential scheme was used to discretize the diffusion terms. In order to reduce the oscillation and keep higher-order accuracy of the numerical solution, a total variation diminishing (TVD) scheme was employed for discretizing the convention term [33, 34]. In this scheme, cell face values are calculated from the combination of upwind scheme part and a central difference anti-diffusive part, which controlled by a smoothness function. In this way, a higher-order discretization scheme is used

10

in smooth regions and reduce to the first order at local extrema of the solution. The upwind part is treated fully implicitly while the anti-diffusive part is treated explicitly. The SIMPLE algorithm for multiphase flow is selected for the pressure-velocity coupling [23, 24]. Due to the strong coupling of the two phases, the coupling terms are singled out from the discretized transport equations, and then the coupled equations are solved simultaneously by using a coupled solver. All the linear equation systems are solved by the preconditioned Bi-conjugate gradient (BCG) algorithm.

4. Results and discussion

4.1. Model validation

For validating the interconnected model for the CLC process, the reported experimental data from Bischi et al.[20] was used. But in their experiments, only axial pressures along the reactors were measured. In order to characterize the capabilities of the model, another set of experimental data from another CFB system documented by Miller and Gidaspow [35] is simulated to test the hydrodynamic behaviours of a single riser. Details of the experimental conditions of the two systems are summarized in table 2 and 3, respectively. Other relevant simulation parameters are listed in table 4. The simulations were run for 30 s of real simulation time and the time average was taken in the period from 10 s to 30 s.

4.1.1. Validation for single CFB model

The governing equations used in the single riser model are the same as those used for the coupled CFB model developed above except the calibration parameter C in drag force model is 0.3. That is because the particle used for the single CFB model validation is different with the one used in the DLCFB model. The calibration parameter value can be adjusted and determined by comparing the calculated results with the experimental axial pressure drop and radial solid volume fraction data. Once the value C is determined for one kind

11

of particle, the parameter is fixed for the simulations with different operation conditions. The entry mass flux of the particles are set equal to the mass flux at the outlet to ensure all particles leaving the riser could be circulated back to the system.

Figure 3 shows the calculated radial profiles of solid volume fraction and their comparison with experimental data. Three riser sections, at 1.86 m, 4.18 m, and 5.52 m above the flow distributor, have been investigated. At 1.86 m above the inlet, Miller [35] reported that the riser is closely packed in a bubbling flow situation. Since the different inlet conditions between the experimental and calculated situation, it is reasonable to believe that there might be some discrepancies at the lowest section. When the height reaches 4.18 m and 5.52 m, the predicted results generally agree with the measured data. However, the simulations clearly illustrate the inherent core-annular pattern of the solids flow. That is the particle concentrations are low in the center and high near the walls.

Figure 4 shows the computed and measured radial distribution of axial solids velocities. The simulation results show a similar distribution which generally fits with the experimental results although the simulated velocities were slightly underpredicted at the upper section of the riser. In addition, the velocity profiles in the upper section are smoother than at the low region which is also captured in the simulation, this phenomena might be due to the retardation in the core velocity.

4.1.2. Validation for coupled DLCFB model

During the DLCFB experiment, a certain amount of the particles were present between the two reactors, so the initial inventory used in the simulations was calculated from the pressure drop between the reactor bottom and top from the experimental data.

Figure 5 and Figure 6 display the predicted axial profile of the pressure compare with the experimental measurement in the FR and AR, respectively. Two different operating gas velocities (a) $v_{g,AR} = 2.1 m/s, v_{g,FR} = 1.8 m/s$ and (b) $v_{g,AR} = 2.6 m/s, v_{g,FR} = 3.2 m/s$ were applied when validating the model.

12

It can be seen that very good agreement was achieved for both reactors and only minor discrepancies occurred in the lower regions of the reactors, close to the inlets. The simulations were not expected to do well in these regions for two reasons. One reason for the deviations may be the simplified gas distribution used at the inlet, which is not strictly consist with the experiment. Besides, the simplified cylindrical shape of the bottom of the reactors may be another contributor to the difference. In general, the comparison between calculated results and the experimental data indicating the interconnected method used in this work is applicable for predicting the performance of DLCFB reactor system.

4.2. Flow characteristics in the DLCFB

A reference case is simulated in this section. The superficial velocity of the FR and AR are 2.6 m/s and 2.4 m/s, respectively. Flow characteristics of the DLCFB reactor system including the solid concentration distribution and velocity distribution are examined.

The solid volume fraction profile of the DLCFB along the reactors height is illustrated in Figure 7. The dense and dilute regions can be observed. The solids accumulate in the bottom of the reactors and the solid volume fraction profile decrease exponentially along the height until the profile is reaching a constant value at the upper parts, below 2 %. So from this figure, it can be seen that both reactors are operated in the transition flow regime between the fast fluidization and the turbulent regime.

Figure 8 shows the time-averaged radial profiles of solids volume fraction and axial velocity at different axial position above the entrance. A typical core-annulus particle distribution was established at different axial positions. The solids mainly accumulate and move downwards at the walls, whereas a dilute gas-solid stream flows upwards in the core of the riser. The flows are fully developed in the upper section of the reactors. Since both reactors are operating in the same fluidization regime, similar trends can be observed in both the FR and the AR. The radial solid distribution in the AR is more flat in the core region compared to the distribution in the FR, which is because the

13

diameter of the AR is larger than the FR.

4.3. Effect of gas superficial velocity

The gas superficial velocity is crucial for the gas-solid interaction and the solid exchange between the FR and the AR. An issue which is challenging in the chemical looping combustion is the maximization of the fuel conversion. The oxygen carrier oxidation has always been an easy task because of the faster oxidation kinetics in the AR than the reduction kinetics in the FR finalizing the fuel conversion. For this reason, the AR operation was kept the same and not changed whereas several superficial gas velocities of the FR were used to investigate the effect of increasing the FR gas velocity.

The effect of changes in the FR velocity on the solid concentration profile is shown in Figure 9. As expected the increment in fuel reactor velocity caused lower solid concentration in the bottom region and higher solid concentration in the upper zone, which is due to the increased drag force with the increasing superficial velocity. In the AR, the solid concentration is not sensitive to the gas velocity in FR since the inlet gas velocity of the AR has maintained. The same phenomena also were observed in the experiments conducted by Bischi et al.[20].

Figure 10 shows the averaged mass flow at the outlet of the two reactors. It is seen that the solid outlet flow in the FR raised, which is the consequence of a high concentration increase in the FR upper part. Whereas the values are almost constant in the AR. The amount of exchanged solid between the reactors is determined by the lower solid flow rate. So in the current operating conditions, the increased gas velocity in the FR enhanced the solid exchanges between the reactors. However increasing the FR gas velocity has the drawback of reducing the FR residence time, which might results in lower conversion of fuel.

4.4. Effect of total solid inventory

Another parameter which can be used to control the system performance is the total solid inventory (TSI). For this reason it is important to understand how

the reactor system responds to TSI variations. The same fluidization conditions were tested with four different inventories.

The variation of the axial solid volume fraction profiles with the TSI are shown in Figure 11. The increased solid mainly accumulated in the lower part. The inflection point from dense region to dilute region is affected significantly by the TSI. When increasing the TSI, the inflection point will move upward. However the solid concentration is almost constant in the upper part, which results the averaged mass flow at the outlet are not sensitive to the increasing TSI, as shown in Figure 12. In addition, the flows within the two reactors are operated in the transition regime between the fast fluidization and the turbulent regime when the TSI is changed. Since the oxygen carriers are costly, further investigations are needed in order to optimise the amount of oxygen carrier required in the reactive system to maximum fuel conversion while minimizing the TSI.

5. Conclusion

A two-fluid model with a kinetic theory of granular flow closure was developed to predict the behaviour of an interconnected DLCFB which can be applied to the CLC system. The configuration of the system consists of two reactors, the air reactor and the fuel reactor. Both reactors are operating in the fast fluidization regime. The model simulates each reactor separately and connect the two reactors through specific boundary conditions, in which the solid flow at the inlet of one reactor was set equal to the solid outlet flow of the other reactor. First, the model was validated against the experimental data obtained from a DLCFB system and a CFB system published in [20] and [35], respectively. The predicted results show good agreement with the measured data as well as the typical core-annulus flow characteristics of the riser can be observed, so the model is found to be applicable for predicting the performance of the system. The effects of operating conditions have been investigated. When increasing the FR superficial gas velocity, more particles in the FR were entrained into the

15

upper part of reactor which result in an increase in the outlet mass flow, indicating that the solid exchanged between the reactors was enhanced. When the total solid inventory was increased, the additional particles are more likely to accumulate at the bottom of both reactors. The model is sufficient for cold flow simulations. Further work continues to implement the reactive CLC system.

Acknowledgments

Nomenclatures

C	calibration parameter
C_1, C_2, C_b, C_μ	turbulence model parameter
d_p	particle diameter, m
e	coefficient of restitution
$\vec{F}_D$	drag force, $kg/m^2 s^2$
$\vec{g}$	gravity acceleration, m/s^2
g_0	radial distribution function
$\bar{\bar{\mathrm{I}}}$	unit tensor
k_g	gas turbulent kinetic energy, m^2/s^2
$\vec{M}_k$	interfacial momentum transfer of phase k, $kg/m^2 s^2$
p_k	pressure of phase k, Pa
r	radial coordinate, m
Re_p	particle Reynolds number
S_t	turbulent kinetic energy production, $kg/m^2 s^2$
t	time s
U	superfical gas velocity m/s
$\vec{v}_k$	velocity of phase k, m/s
z	axial position above the inlet, m

Greek letters

α_k	volume fraction of phase k
β	interfacial drag coefficient
γ_s	collisional energy dissipation, $kg/m^3 s$
ε_g	turbulent energy dissipation rate, m^2/s^3
κ_s	conductivity of granular temperature, kW/mK
μ_k	viscosity of phase k, $Pa \cdot s$
ρ_k	density of phase k, kg/m^3
$\bar{\bar{\tau}}_k$	stress tensor of phase k, Pa
$\bar{\bar{\tau}}_t$	turbulent stress tensor, Pa
Θ	granular temperature, m^2/s^2

superscripts

$dilute$	dilute
max	maximum

subscripts

AR	air reactor
B	bulk
FR	fuel reactor
g	gas phase
s	solid phase
t	turbulent

References

[1] IPCC, Climate Change 2014: Mitigation of Climate Change, Vol. 3, Cambridge University Press, New York, US, 2015.

[2] H. Yang, Z. Xu, M. Fan, R. Gupta, R. B. Slimane, A. E. Bland, I. Wright, Progress in carbon dioxide separation and capture: A review, J. Environ. Sci. 20 (1) (2008) 14–27.

[3] J. Adanez, A. Abad, F. Garcia-Labiano, P. Gayan, F. Luis, Progress in chemical-looping combustion and reforming technologies, Prog. Energy Combust. Sci. 38 (2) (2012) 215–282.

[4] A. Nandy, C. Loha, S. Gu, P. Sarkar, M. K. Karmakar, P. K. Chatterjee, Present status and overview of chemical looping combustion technology, Renew. Sustainable Energy Rev. 59 (2016) 597–619.

[5] J. Jung, I. K. Gamwo, Multiphase cfd-based models for chemical looping combustion process: fuel reactor modeling, Powder Technol. 183 (3) (2008) 401–409.

[6] Z. Deng, R. Xiao, B. Jin, Q. Song, H. Huang, Multiphase cfd modeling for a chemical looping combustion process (fuel reactor), Chem. Eng. Technol. 31 (12) (2008) 1754–1766.

[7] Z. Deng, R. Xiao, B. Jin, Q. Song, Numerical simulation of chemical looping combustion process with caso 4 oxygen carrier, Int. J. Greenh. Gas Control 3 (4) (2009) 368–375.

[8] B. Jin, R. Xiao, Z. Deng, Q. Song, Computational fluid dynamics modeling of chemical looping combustion process with calcium sulphate oxygen carrier, Int. J. Chem. Reactor Eng. 7 (1) (2009) A19.

[9] H. Kruggel-Emden, F. Stepanek, A. Munjiza, A study on the role of reaction modeling in multi-phase cfd-based simulations of chemical looping combustion, Oil & Gas Sci. Technol. 66 (2) (2011) 313–331.

19

[10] K. Mahalatkar, J. Kuhlman, E. D. Huckaby, T. O'Brien, Computational fluid dynamic simulations of chemical looping fuel reactors utilizing gaseous fuels, Chem. Eng. Sci. 66 (3) (2011) 469–479.

[11] H. Kruggel-Emden, S. Rickelt, F. Stepanek, A. Munjiza, Development and testing of an interconnected multiphase cfd-model for chemical looping combustion, Chem. Eng. Sci. 65 (16) (2010) 4732–4745.

[12] S. Wang, H. Lu, F. Zhao, G. Liu, Cfd studies of dual circulating fluidized bed reactors for chemical looping combustion processes, Chem. Eng. J. 236 (2) (2014) 121–130.

[13] A. Bougamra, L. Huilin, Modeling of chemical looping combustion of methane using a ni-based oxygen carrier, Energy Fuels 28 (5) (2014) 3420–3429.

[14] S. Banerjee, R. K. Agarwal, An eulerian approach to computational fluid dynamics simulation of a chemical-looping combustion reactor with chemical reactions, Journal of Energy Resources Technology 138 (4) (2016) 042201.

[15] Y. Guan, J. Chang, K. Zhang, B. Wang, Q. Sun, Three-dimensional cfd simulation of hydrodynamics in an interconnected fluidized bed for chemical looping combustion, Powder Technol. 268 (2014) 316–328.

[16] C. Geng, W. Zhong, Y. Shao, D. Chen, B. Jin, Computational study of solid circulation in chemical-looping combustion reactor model, Powder Technol. 276 (2015) 144–155.

[17] J. M. Parker, Cfd model for the simulation of chemical looping combustion, Powder Technology 265 (2014) 47–53.

[18] M. A. Hamilton, K. J. Whitty, J. S. Lighty, Numerical simulation comparison of two reactor configurations for chemical looping combustion and chemical looping with oxygen uncoupling, J. Energy Resour. 138 (4) (2016) 042213.

[19] T. Pröll, P. Kolbitsch, J. Bolhàr-Nordenkampf, H. Hofbauer, A novel dual circulating fluidized bed system for chemical looping processes, AlChE J. 55 (12) (2009) 3255–3266.

[20] A. Bischi, Ø. Langørgen, J.-X. Morin, J. Bakken, M. Ghorbaniyan, M. Bysveen, O. Bolland, Hydrodynamic viability of chemical looping processes by means of cold flow model investigation, Appl. Energy 97 (2012) 201–216.

[21] H. Enwald, E. Peirano, A. E. Almstedt, Eulerian two-phase flow theory applied to fluidization, Int. J. Multiphase Flow 22 (1996) 21–66.

[22] J. Ding, D. Gidaspow, A bubbling fluidization model using kinetic theory of granular flow, AlChE J. 36 (4) (1990) 523–538.

[23] H. Lindborg, Modeling and Simulation of Reactive Two-Phase Flows in Fluidized Bed Reactors, Ph.D. thesis, Norwegian Institute of Technology, Trondheim, Norway (2008).

[24] H. A. Jakobsen, Chemical Reactor Modeling, 2nd Edition, Springer-Verlag, Multiphase Reactive Flows, Berlin, Germany: Springer-Verlag, 2014.

[25] L. Gibilaro, R. Di Felice, S. Waldram, P. Foscolo, Generalized friction factor and drag coefficient correlations for fluid-particle interactions, Chem. Eng. Sci. 40 (10) (1985) 1817–1823.

[26] T. McKeen, T. Pugsley, Simulation and experimental validation of a freely bubbling bed of fcc catalyst, Powder Technol. 129 (1) (2003) 139–152.

[27] H. A. Jakobsen, On the modelling and simulation of bubble column reactors using a two-fluid model, Ph.D. thesis, Norwegian Institute of Technology, Trondheim, Norway (May 1993).

[28] J. Ding, D. Gidaspow, A bubbling fluidization model using kinetic theory of granular flow, AlChE J. 36 (4) (1990) 523–538.

[29] D. Gidaspow, Multiphase flow and fluidization: continuum and kinetic theory descriptions, Academic press, San Diego, US, 1994.

[30] J. Jenkins, S. Savage, A theory for the rapid flow of identical, smooth, nearly elastic, spherical particles, J. Fluid Mech. 130 (1983) 187–202.

[31] D. Ma, G. Ahmadi, An equation of state for dense rigid sphere gases, J. Chem. Phys. 84 (6) (1986) 3449–3450.

[32] C. Lun, S. B. Savage, D. Jeffrey, N. Chepurniy, Kinetic theories for granular flow: inelastic particles in couette flow and slightly inelastic particles in a general flowfield, J. Fluid Mech. 140 (1984) 223–256.

[33] B. van Leer, Towards the ultimate conservation difference scheme. ii. monotonicity and conservation combined in a second-order scheme, J. Comput. Phys. 14 (1974) 361–370.

[34] B. van Leer, Towards the ultimate conservative difference scheme. iv. a new approach to numerical convection, J. Comput. Phys. 23 (3) (1977) 276–299.

[35] A. Miller, D. Gidaspow, Dense, vertical gas-solid flow in a pipe, AlChE J. 38 (11) (1992) 1801–1815.

Table 1

Empirical parameters for the $\kappa - \varepsilon$ model [24].

C_μ	σ_0	σ_ε	C_1	C_2	C_b
0.09	1.00	1.30	1.44	1.92	0.25

Table 2

Main geometric and operating parameters for DLCFB [20].

Description	Unit	Value
Reactor geometry		
AR height	m	5
AR diameter	m	0.23
FR height	m	5
FR diameter	m	0.144
Particle properties		
Mean particle size	μm	50
Particle density	kg/m^3	7000
Operational condition		
Operating pressure	atm	1.0
Operating temperature	K	293
Gas superficial velocity of AR	m/s	2.1-2.6
Gas superficial velocity of FR	m/s	1.8-3.2

Table 3

Main geometric and operating parameters for CFB [35].

Description	Unit	Value
Reactor geometry		
CFB riser height	m	6.6
CFB riser diameter	m	0.075
Particle properties		
Mean particle size	μm	75
Particle density	kg/m^3	1654
Operational condition		
Operating pressure	atm	1.0
Operating temperature	K	293
Gas superficial velocity of inlet	m/s	2.61

Table 4

simulation parameters.

Description	Unit	Value
grid size	–	$0.0048 \times 0.02\ m$
Gas viscosity	$kg\ m^{-1}s^{-1}$	1.82×10^{-5}
Gas density	kg/m^3	1.2
Sphericity of particle	–	1
Restitution coefficient of particles	–	0.99
Time step	s	1.0×10^{-4}
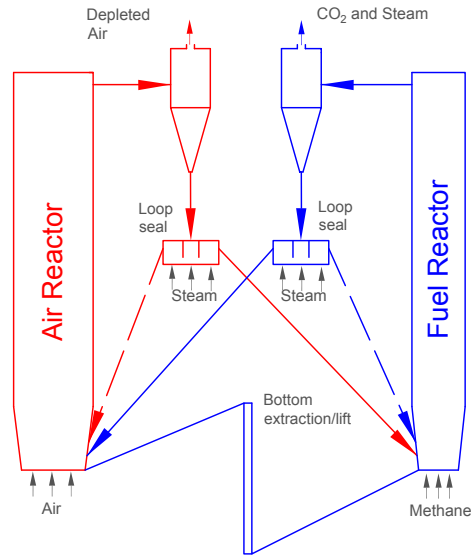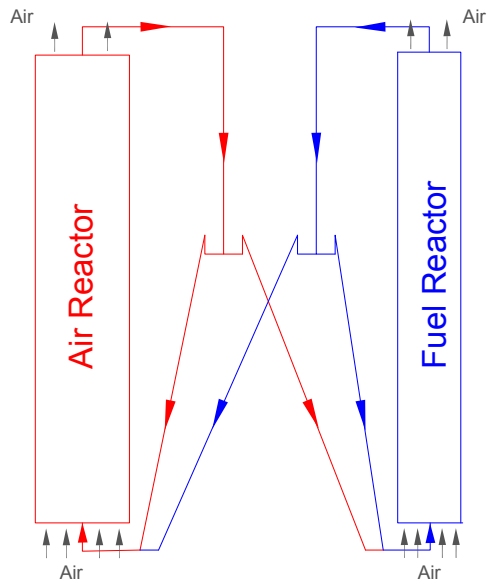
Figure 1: (a)Sketch of the double loop circulating fluidized bed reactor [20]. (b) Schematic of the 2D computational domain
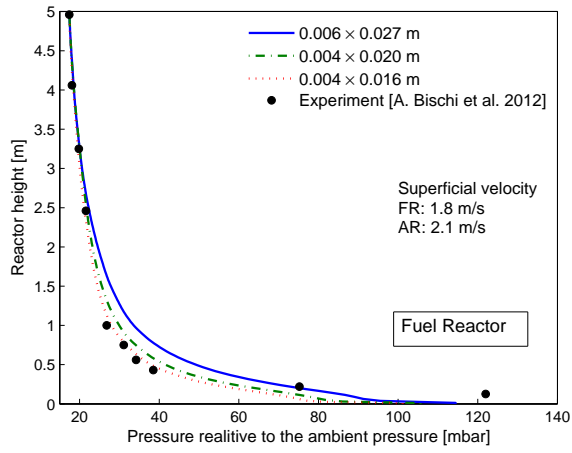
(a)
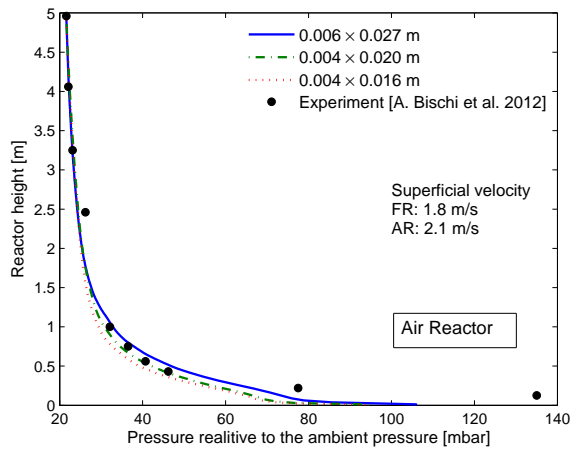
(b)

Figure 2: Comparison of pressure profiles along the height of the FR and the AR with different grid numbers
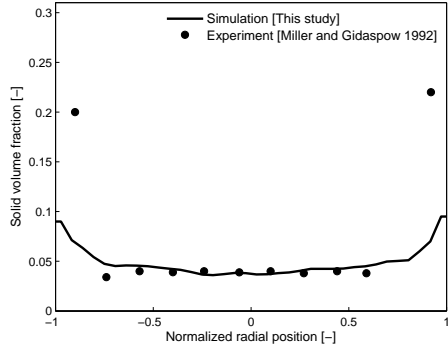
(a)
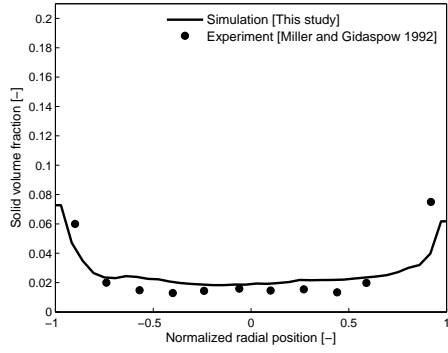
(b)
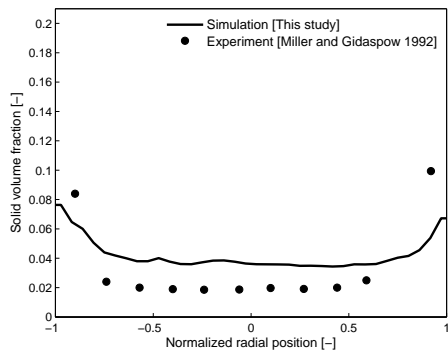
(c)

Figure 3: Comparison of the radial distribution of solid volume fraction between simulation and experiment results. (a) z=1.86 m; (b) z=4.18 m; (c) z=5.52 m.
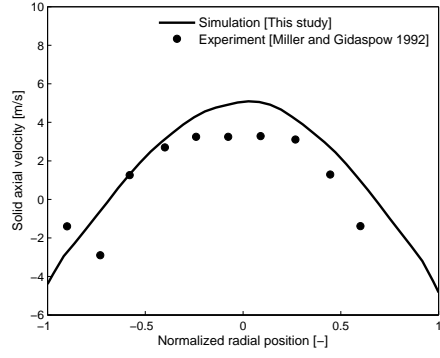
(a)
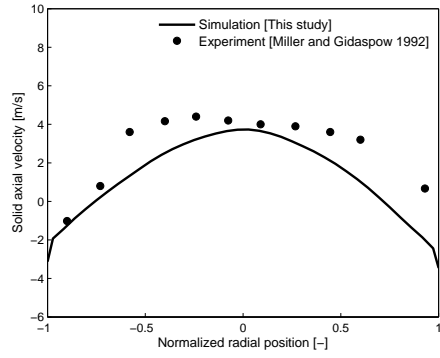
(b)
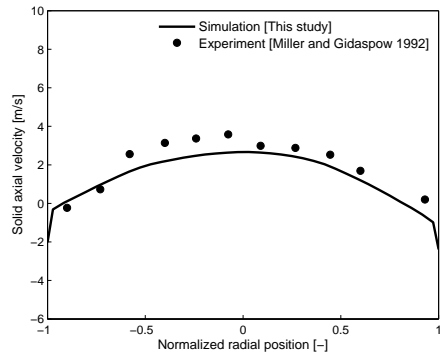
(c)

Figure 4: Comparison of the axial solid velocity between simulation and experiment results.
(a) z=1.86 m; (b) z=4.18 m; (c) z=5.52 m.

28
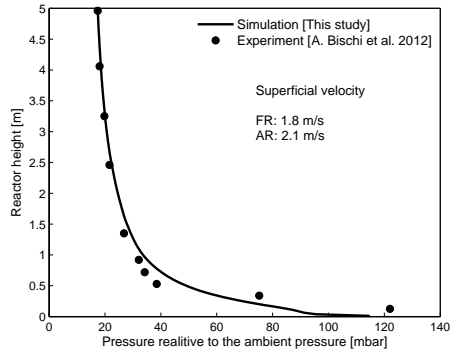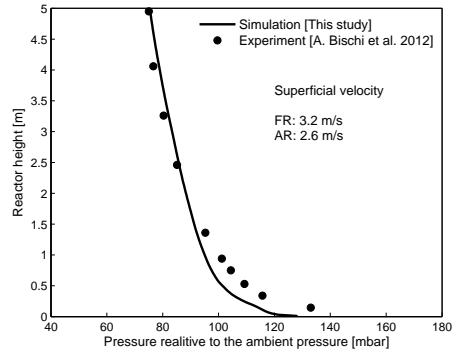
(a)   (b)

Figure 5: Comparison of pressure profiles in FR between simulation and experiment results
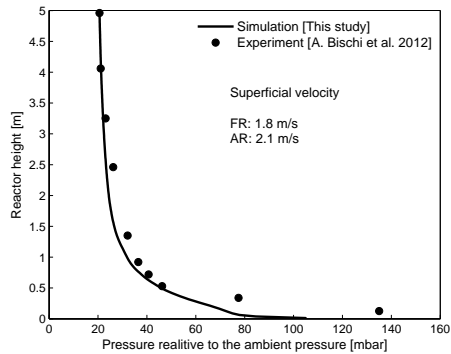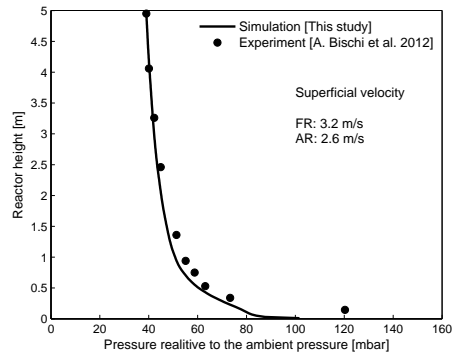
(a)   (b)

Figure 6: Comparison of pressure profiles in AR between simulation and experiment results
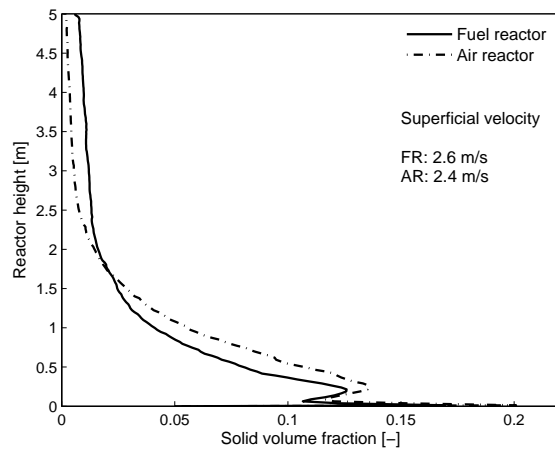
Figure 7: Axial profile of time-averaged solids volume fraction
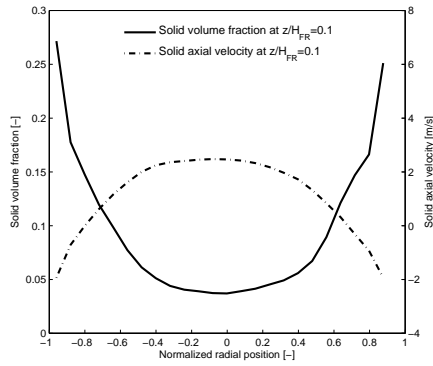
(a)
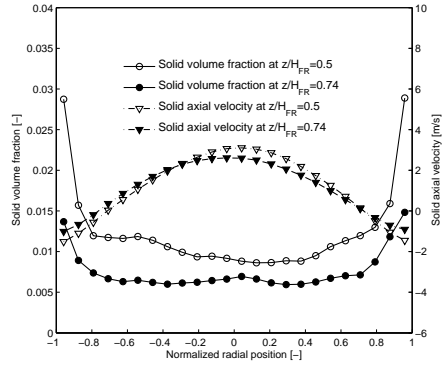
(b)
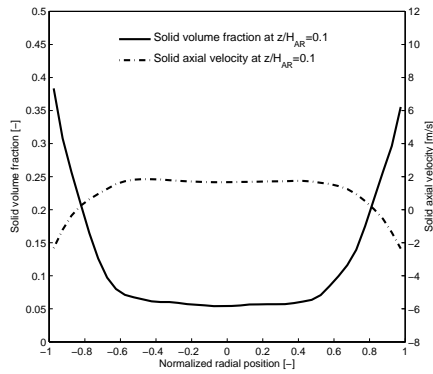
(c)
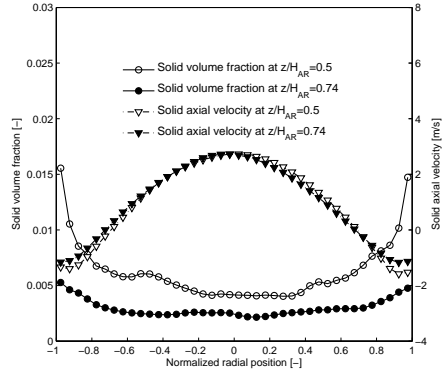
(d)

Figure 8: Radial distribution of solid volume fraction and axial solid velocity of the FR (a,b) and AR (c,d) (conditions: $U_{FR} = 2.6$, $U_{AR} = 2.4$)

(a)   (b)
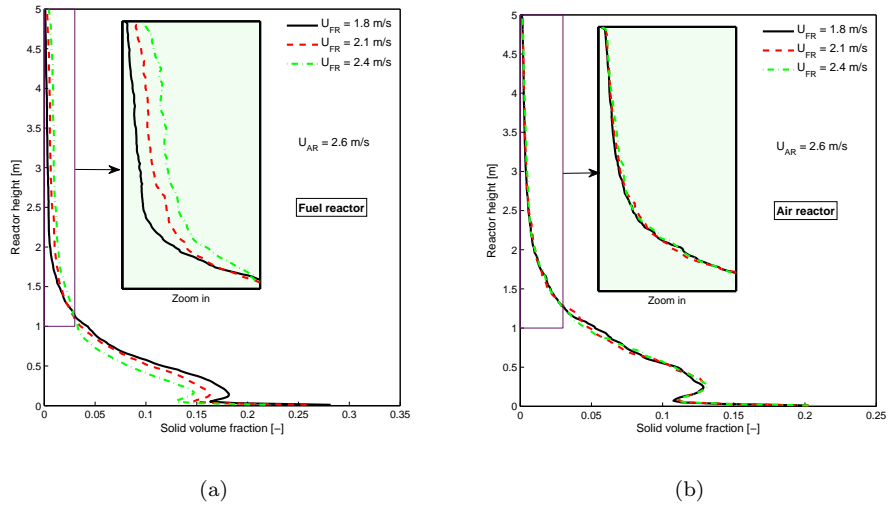
Figure 9: Effect of superficial gas velocity in FR on the solid volume fraction along the height of both reactors
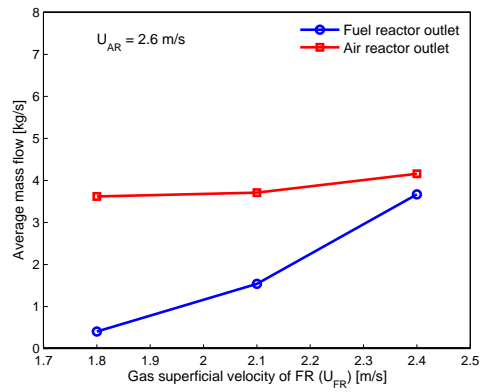

Figure 10: Effect of superficial gas velocity in FR on the averaged mass flow at outlets of reactors
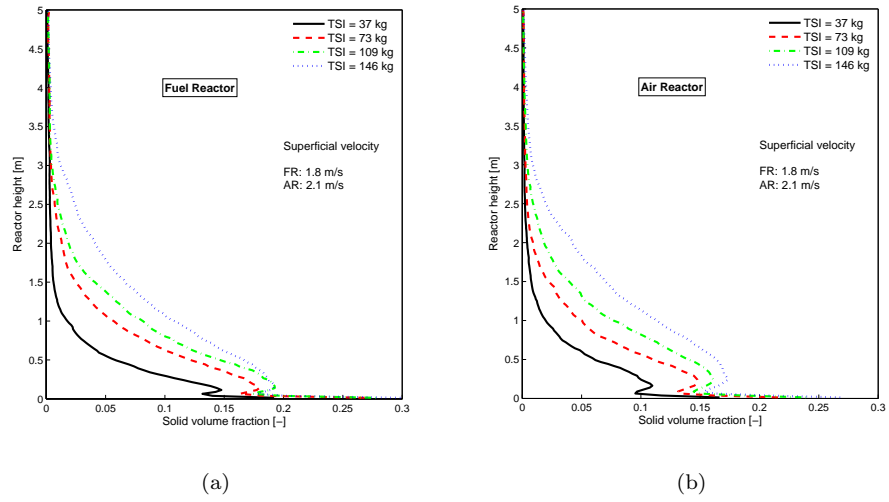
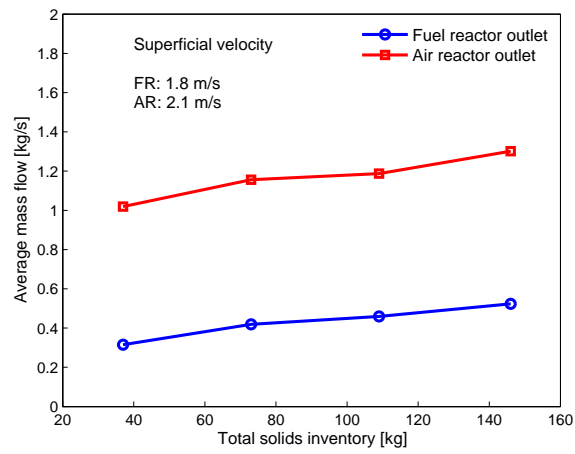Figure 11: Effect of TSI on the solid volume fraction along the height of reactors

Figure 12: Effect of TSI on the averaged mass flow at outlets of reactors

33